ELSEVIER

Surface Science 342 (1995) 233–249

surface science

UHV transmission electron microscopy structure determination of the Si(111)-($\sqrt{3} \times \sqrt{3}$)R30°Au surface

Richard Plass *, Laurence D. Marks

Department of Materials Science and Engineering, Northwestern University, Evanston, IL60208, USA

Received 23 January 1995; accepted for publication 20 June 1995

Abstract

Details of the average atomic structure and the possible nature of the surface domain walls of the Si(111)-$\sqrt{3} \times \sqrt{3}$)R30°Au surfaces are presented. Transmission electron diffraction data supports the missing top layer twisted trimer [Surf. Sci. 256 (1991) 135] model in which gold and silicon atoms in the top two layers form sets of like-atom trimers rotated in the same direction about p3 symmetry centers. However, the average degree of trimer rotation and the interatomic spacings within the structure vary significantly with the sharpness of the structure's diffraction spots. These variations in structure parameters among data sets as well as large values of the fitted Debye–Waller terms indicate substantial static disorder in the structure and hence any parameters determined can only be averages of locally varying parameters. Silicon displacements from the bulk positions continue through the second silicon double layer. Charge transfer in the structure is evident from a better fit obtained using Au^+ scattering factors than with those for neutral gold, confirming a total energy cluster calculation [Surf. Rev. Lett. 1 (1994) 273]. The presence of gold trimers is confirmed by the local symmetry seen in high resolution micrographs which also show surface domain morphology differences between diffuse and sharp diffraction spot regions. These images additionally indicate that the surface domain walls must be either vacancy type, or the gold-to-gold spacing in and near the walls must be close to 3.84 Å. From these observations, models for the Si(111)-($\sqrt{3} \times \sqrt{3}$)R30°Au domain walls and the Si(111)-(6 × 6) Au structure are proposed.

Keywords: Computer simulations; Gold; Low index single crystal surfaces; Semiconducting surfaces; Si(111)-($\sqrt{3} \times \sqrt{3}$) R30°Au; Silicon; Surface defects; Surface structure; Transmission electron microscopy; Transmission high-energy electron diffraction

1. Introduction

Over the past few decades, the Si(111)-($\sqrt{3} \times \sqrt{3}$)R30°Ag structure ([3,4], and references therein) has received considerable interest in the literature as a prototypical Si(111)-($\sqrt{3} \times \sqrt{3}$)R30°-metal-type structure, which several metals form after annealing when present in submonolayer coverages on the Si(111) surface. Less well understood is the Si(111)-($\sqrt{3} \times \sqrt{3}$)R30°Au surface (denoted hereafter as $\sqrt{3}$-Au). First observed by Bishop and Riviere [5] using low energy electron diffraction (LEED), the $\sqrt{3}$-Au structure coexists with the Si(111)-(5 × 2) Au structure at elevated temperatures for coverages between 0.5 to 0.8 monolayers (one monolayer $\sim 7.8 \times 10^{14}$ gold atoms per cm^2). Although above 0.8 ML the surface is completely covered with $\sqrt{3}$-Au, 0.8 ML is not necessarily the saturation coverage since the $\sqrt{3}$-Au structure accommodates more gold up to about 1.0 monolayer after which the Si(111)-(6 × 6) Au structure appears [6–10]. Several authors have noted that within the 0.5 to 1.0 ML coverage and 200 to 800°C temperature ranges a variety of

* Corresponding author. Fax: +1 708 4917820.

0039-6028/95/$09.50 © 1995 Elsevier Science B.V. All rights reserved
SSDI 0039-6028(95)00739-3

shapes for the $\sqrt{3}$-Au diffraction spots can be observed. Sharp spots, diffuse spots, arcs partially surrounding sharp spots, and hexagonally symmetric star-shaped spots have been reported [6,7,11]. These features are likely related to the relatively small sizes of the surface domains which are on average 7 to 8 $\sqrt{3}$-Au unit cells (approximately 50 Å) in diameter [8]. The STM work of Takami et al. [9], in which the relative coverages of two apparently different $\sqrt{3}$-Au phases were measured as a function of total gold coverage, supports the speculation of Ino and also Takayanagi of two different $\sqrt{3}$-Au phases [7,11] and makes it clear that a thorough understanding of the atomic structures of any surface phases present is needed to understand the dynamics of this system.

Several studies are of relevance to the $\sqrt{3}$-Au atomic structure: STM data [8,9,12–15] typically shows a single bright feature per unit cell forming a hexagonal pattern. In at least one study this bright spot had triangular features [13]. Bishop and Riviere, from their LEED data, initially proposed a 1/3 ML coverage model with one gold atom per unit cell [5]. Lelay and coworkers [16] proposed a triplet overlayer model based on Auger electron spectroscopy and LEED. Using impact-collision ion scattering spectroscopy (ICISS) Oura et al. [17] proposed a modified triplet coplanar model which consists of a 1 ML triplet layer of gold over a 2/3 ML honeycomb of silicon. Also using ICISS Huang and Williams [18] proposed a mixed model consisting of a 2/3 ML gold honeycomb structure with some cells having gold in the unit centers. Based on medium energy ion scattering data, Chester and Gustafsson [1] proposed a missing top layer twisted trimer model (MTLTT) in which a layer of gold takes the place of the first layer of silicon atoms in the top double layer of the Si(111) surface. The gold and silicon atoms in these top two layers of the structure both form trimer groups which rotate about the centers of the trimers. Two possible models were proposed based on whether the silicon trimers rotate about their centers in the same direction or in the opposite direction as the gold trimers. Akiyama et al. [19] also suggested the $\sqrt{3}$-Au structure could be based on twisted trimers based on their TEM results of the Si(111)-($\sqrt{3} \times \sqrt{3}$) Pd surface. Chester and Gustafsson also pointed out the likelihood of significant distortions in the silicon layers immediately below the surface. X-ray diffraction data [20] from Dornisch et al. partially support the MTLTT models in also showing a missing top layer trimer structure and "splitting" of the second layer silicon sites. This splitting essentially forms silicon trimers given the constraints of symmetry. Dornisch et al. saw no rotation of the gold trimers and did not propose a registry of the surface structure with the bulk. Their data also point to the likelihood of substantial subsurface distortions. The theoretical work of Ding and coworkers [21], based on total energy calculations, gives the conjugate honeycomb chained trimer (CHCT) model whose dominant features are a missing silicon top layer, gold trimers with no rotation, and first layer silicon atoms equidistant from all the nearest gold atoms. The CHCT model is essentially the MTLTT model without any twists and hence preserves the mirror planes of p3m1 symmetry which they conclude the structure must obey. This model is supported by the dynamical LEED structure analysis of Quinn et al. [22] and by the recent X-ray diffraction work of Kuwahara et al. [23]. The missing top layer feature of both the MTLTT and CHCT models is supported by the low temperature hole–island pair growth mechanism for the $\sqrt{3}$-Au structure proposed by Shibata and coworkers [15]. They have observed that between 200 and 280°C, gold deposited on the Si(111)-(7 × 7) structure will form adjacent domains of $\sqrt{3}$-Au surfaces with a z-axis difference between them equal to the Si(111) surface step height. This can be understood in terms of Si atoms diffusing from a "hole" or defective region of the 7 × 7 surface and combining with gold diffusing on the surface to form a $\sqrt{3}$-Au "island" nearby and one surface step up from the original surface. Simultaneously, gold also diffuses onto the now silicon deficient surface of the 7 × 7 "hole" to form another $\sqrt{3}$-Au surface there. Similar hole–island features have recently been reported for the gold on germanium system [24]. Finally, a recent total energy cluster calculation of the $\sqrt{3}$-Au system [2] assuming gold in the H_3-type site predicts a charge transfer of 0.8 units of electron charge from the gold to the silicon.

Given the contradicting results, outlined above, concerning the $\sqrt{3}$-Au structure, we have investigated it using the unique capabilities of plan-view transmission electron microscopy [25–28]. Transmission electron diffraction (TED) is very sensitive to atomic displacements perpendicular to the electron beam for the surface layers, the relaxation layers and the bulk crystal. High resolution electron microscopy (HREM) from surfaces provides detailed local atomic information based on atomic scattering alone. Details of the Hitachi UHV-H9000 300 kV instrument used in this study have been reported elsewhere [29,30].

2. Experimental

Thinned TEM samples of p-type (~ 10 Ω·cm) Si(111) were prepared ex situ by mechanical polishing and HF solution chemical etching. Under UHV conditions the samples were further thinned to electron transparency (roughly 30 nm) by cycles of 2.5 kV Ar^+ ion milling and electron beam annealing. The two Si(111) surfaces were also cleaned and ordered by this treatment until no contamination (mainly C and O) peaks were visible using parallel electron energy loss spectroscopy and there was a very low number of impurity islands in the images. Well-defined Si(111)-(7 × 7) diffraction patterns were visible from these surfaces. Roughly 0.7 ML of gold was evaporated onto one surface (the top for the imaging studies, the bottom for the diffraction studies) with the samples held at room temperature. The gold deposition was measured with a quartz crystal microbalance and during deposition the base pressure did not exceed 1×10^{-9} Torr. After deposition the samples were lightly electron beam annealed to form the $\sqrt{3}$-Au surface. All TEM observations were carried out at room temperature and to limit electron beam damage effects the HREM and bright field data were collected using a beam voltage of 250 kV while TED data were collected at 250 and 300 kV. Because of the structures' sensitivity to the electron beam knock-on damage, exposure limiting techniques were used in imaging modes, where in general electron doses per unit area are high. The diffraction data are essentially unaffected by beam damage since the electron doses per unit area are much lower.

3. Diffraction analysis

Figs. 1a and 1b show typical off zone transmission electron diffraction patterns of the $\sqrt{3}$-Au structure used in the atomic structure analysis. To collect as much information as possible, three sets of through exposure series diffraction patterns were recorded with different sample tilts and thickness. The first two of these exposure series had rather diffuse diffraction spots, as shown in Fig. 1a, while the third had fairly sharp spots, as shown in Fig. 1b. The diffraction data sets were quantified by first digitizing the negatives using an Optronics P1000 microdensitometer followed by analysis using a cross-correlation intensity analysis routine written within SEMPER imaging software [31].

The data from all the negatives were combined in a three step process to obtain the beam intensities and errors. First, initial relative exposure levels of the negatives were determined by a least-squares fit using beams which occurred in more than one negative. (These exposure levels were close to those separately determined from the exposure times.) Then these initial exposure values were used to obtain a first estimate of the mean intensity of each beam, and from this the intensity error of each beam, in each negative. From previous work [31] we know that the errors obey counting statistics, so for any given negative the standard deviation of the errors will be some constant scaling term times the intensity of each beam. From the distribution of errors these scaling terms (essentially better estimates of the exposure levels) were determined and an improved estimate of the weighted mean intensity was then determined. After iterating this process a few times the results converged to give a set of mean intensity measurements per negative, each with a known standard deviation. The final step used these values in a conventional fashion to determine the beam intensities and standard deviations. We would estimate that this procedure is several times more

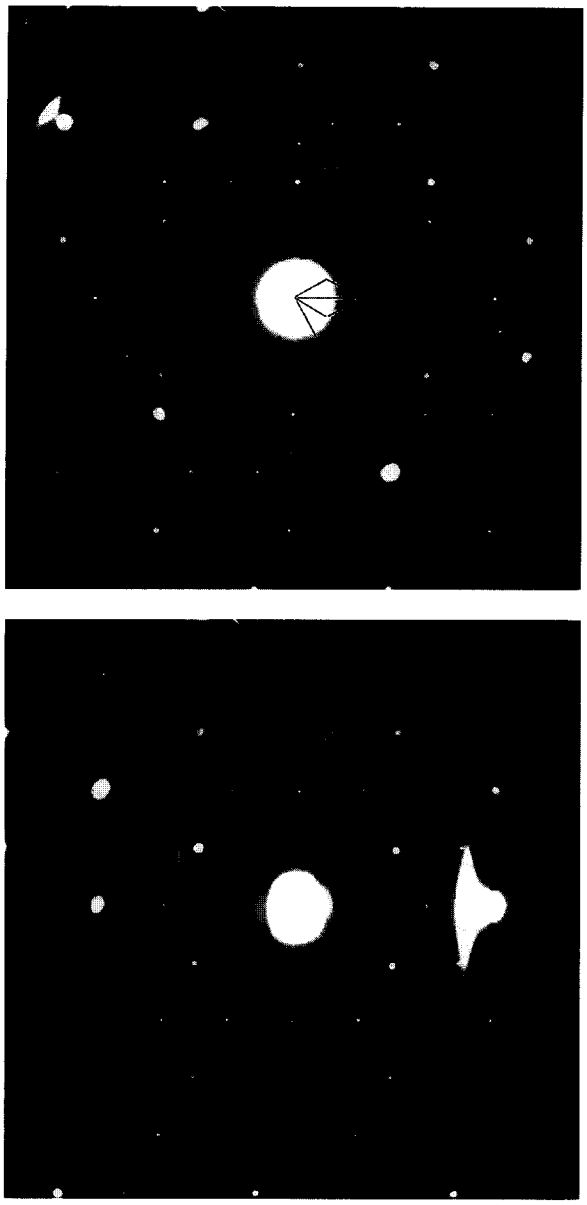

Fig. 1. Typical experimental off zone diffraction patterns of the Si(111)-($\sqrt{3}\times\sqrt{3}$) Au surface with (a) diffuse and (b) sharp diffraction spots. In (a) the ($\sqrt{3}\times\sqrt{3}$) and (1×1) unit cells are indicated by the smaller and larger rhombuses, respectively, while the strong {21} beams referred to in Table 1 are indicated with arrows in (b). The positions of three of the six much weaker {20} beams are indicated with circles.

accurate than what we have used previously [28,31], since we are exploiting repeat measurements to determine the errors. The above analysis of repeated measurements rather than using other members of an exposure series to "fill in" data missing due to nonlinear exposure regions of a single exposure also separates this study from similar TED-based studies of Si(111)-(7×7) [25,32], Si(111)-($\sqrt{3}\times\sqrt{3}$)R30°B [33], and Ir(100)-(5×1) [34].

The resulting experimental absolute mean intensities of the twelve strongest and selected weaker surface beams in the first and third data sets as well as their standard deviations and theoretical fit values are given in Table 1 and their general locations are indicated in Fig. 1b. (Note that the differences between kinematically equivalent spots is larger than the measurement errors; this is due to the dynamical character of electron diffraction.) The three $\sqrt{3}$-Au electron diffraction data sets have the following number of independent beams, sample tilts and sample thicknesses: Set 1, 264 diffuse beams 118.5 mrad 32.8 nm; Set 2, 73 diffuse beams 46.0 mrad 33.7 nm; Set 3, 297 sharp beams 57.4 mrad 30.9 nm. Since fewer beams were sampled in the second data set its results should in general be considered less reliable than the other two. Reciprocal space locations beyond the beams appearing in the most heavily exposed negative were checked but found to have only a shot-noise background intensity. Hence surface structure beams from just outside the (220) set of bulk beams out to the (10 10 0) bulk beams, which did not have a measured intensity, were set to zero with errors determined from the most heavily exposed negative's variance. This brought the data sets to 530, 332, and 527 beams, respectively.

Theoretical beam intensity values were calculated for various proposed models of the $\sqrt{3}$-Au structure (including the surface and the bulk) using a double precision dynamical multislice method [35]. The parameters of the model were then adjusted to obtain a best χ^2 fit to the experimental data sets using the minimization routine NL2SOL from Netlib [36]. Here χ^2 is defined as

$$\chi^2 = 1/(N-M)\sum[(I_e(g)-I_c(g))^2/\sigma^2(g)], \qquad (1)$$

Table 1
Experimental and calculated intensities relative to the transmitted beam for the twelve strongest and selected weaker beams of the first and third data sets of the Si(111)-($\sqrt{3}\times\sqrt{3}$)R30° Au surface; also included are the absolute and relative standard deviations of the experimental intensities and the quotients of the difference between the experimental and calculated intensity divided by the absolute experimental deviation

Surface h	Index k	Experimental intensity	Calculated intensity	Absolute σ	Relative σ (%)	Δ Intensity/σ
0	0	1.00	1.00			
Set 1 (Diffuse)						
Strongest beams (2,1 type)						
−3	−2	2.02×10^{-4}	1.92×10^{-4}	9.80×10^{-6}	4.85	1.02
−3	−1	2.04×10^{-4}	1.89×10^{-4}	1.03×10^{-5}	5.07	1.45
−2	−3	1.79×10^{-4}	1.72×10^{-4}	9.26×10^{-6}	5.17	0.76
−2	1	1.91×10^{-4}	1.81×10^{-4}	9.71×10^{-6}	5.08	1.03
−1	−3	1.86×10^{-4}	1.59×10^{-4}	9.80×10^{-6}	5.27	2.75
−1	2	2.07×10^{-4}	1.82×10^{-4}	1.01×10^{-5}	4.87	2.48
1	−2	1.74×10^{-4}	1.85×10^{-4}	9.52×10^{-6}	5.47	−1.15
1	3	1.87×10^{-4}	1.68×10^{-4}	9.90×10^{-6}	5.29	1.92
2	−1	1.99×10^{-4}	1.84×10^{-4}	1.02×10^{-5}	5.12	1.47
2	3	1.79×10^{-4}	1.69×10^{-4}	1.08×10^{-5}	6.04	0.93
3	1	2.13×10^{-4}	1.62×10^{-4}	1.24×10^{-5}	5.83	4.11
3	2	1.97×10^{-4}	1.75×10^{-4}	1.04×10^{-5}	5.28	2.12
Set 3 (Sharp)						
Strongest beams (2,1 type)						
−3	−2	9.41×10^{-5}	1.05×10^{-4}	7.46×10^{-6}	7.93	−1.46
−3	−1	1.15×10^{-4}	1.08×10^{-4}	8.85×10^{-6}	7.70	0.79
−2	−3	9.47×10^{-5}	9.28×10^{-5}	6.54×10^{-6}	6.90	0.29
−2	1	1.12×10^{-4}	9.31×10^{-5}	7.41×10^{-6}	6.61	2.55
−1	−3	1.12×10^{-4}	9.45×10^{-5}	7.14×10^{-6}	6.38	2.45
−1	2	1.15×10^{-4}	1.11×10^{-4}	7.04×10^{-6}	6.12	0.57
1	−2	1.22×10^{-4}	9.90×10^{-5}	7.69×10^{-6}	6.31	2.99
1	3	1.10×10^{-4}	1.02×10^{-4}	8.00×10^{-6}	7.27	1.00
2	−1	1.20×10^{-4}	1.07×10^{-4}	7.58×10^{-6}	6.31	1.72
2	3	1.09×10^{-4}	1.08×10^{-4}	7.04×10^{-6}	6.46	0.14
3	1	1.16×10^{-4}	1.03×10^{-4}	7.81×10^{-6}	6.73	1.66
3	2	9.75×10^{-5}	1.09×10^{-4}	7.69×10^{-6}	7.89	−1.50
Weaker beams (2,0 type)						
−2	0	7.63×10^{-6}	3.62×10^{-6}	1.99×10^{-6}	26.06	2.02
0	−2	7.56×10^{-6}	4.22×10^{-6}	1.08×10^{-6}	14.22	3.11
0	2	8.42×10^{-6}	5.52×10^{-6}	1.20×10^{-6}	14.29	2.41
2	0	9.13×10^{-6}	6.47×10^{-6}	1.16×10^{-6}	12.68	2.30
2	2	6.90×10^{-6}	2.62×10^{-6}	1.11×10^{-6}	16.03	3.87

where $\boldsymbol{g}$ is the diffracted beam, $I_e(g)$ is the experimental $I_c(g)$ the calculated intensity, $\sigma(g)$ is the standard deviation of the error associated with each beam $\boldsymbol{g}$, N is the number of diffracted beams and M the number of parameters in the model. For models with two possible domains, a linear combination of intensities from both domains was used for the fit. Parameters (atomic locations and Debye–Waller terms) for various $\sqrt{3}$-Au models were calculated by fitting three combinations: fitting all three data sets to one set of parameters simultaneously, fitting each data set to its own set of parameters, and fitting only the diffuse spot data sets (the first and second) to one set of parameters. The significance of fitting the data sets in these different ways will be explained in the next section. To model the relaxations of the atomic layers going into the bulk a strain field constrained to obey the

equations of inhomogeneous, isotropic elasticity was applied [28,37]. Further details can be found in Ref. [28].

4. Results and discussion

Before discussing the diffraction results of this study a few technical issues need to be addressed. We are dealing with a combination of scattering from gold and silicon. Subtle variations in the silicon spacings, i.e. high angle scattering effects, can easily be masked by variations in the stronger gold scattering unless the (typically very weak) scattering at high angles is known accurately. This issue comes into play when considering the coupling between the occupancy of sites and the thermal and static Debye–Waller terms as will be discussed in more detail below. Unless a detailed temperature study is done of the structure scattering, especially at higher angles, it is nearly impossible to sort out the Debye–Waller effects from small occupancy variations since a lowering on the occupancy of a structure site manifests itself almost identically to an increase in the Debye–Waller term. Fortunately, as discussed below, in this study HREM can be employed to determine the general occupancy of the gold sites. HREM is also used to partially bypass another inherent problem with diffraction data, the fact that scattering from the domain walls will generate a diffuse background diffraction intensity versus any sharp features in the diffraction patterns.

The first column of Table 2 gives the parameters relevant to the MTLTT structure shown in Fig. 2. This structure has a χ^2 of 2.76 from fitting all three data sets simultaneously. The presence of gold trimers on the surface was confirmed by the HREM images in Figs. 3a and 3b, taken near the (111) zone axis. The images have been noise filtered [38] and the contrast from the 220-type bulk fringes attenuated to enhance the information from the $\sqrt{3}$ and 1×1-type fringes. As indicated by the polygons set over patches of the $\sqrt{3}$-Au structure in some areas, both these images show, especially in the domain centers, an apparent local threefold symmetry of the $\sqrt{3}$-Au structure which could only come from a gold trimer structure with a 1 ML saturation coverage. Determining the exact extent of each domain is tricky in on-zone imaging mode because of the need for low pass filtering. In this imaging mode there is also a slim possibility that a sixfold symmetric structure and certain (unlikely) imaging conditions could also generate nearly threefold symmetric image features. Experiments are currently underway to verify unambiguously the local symmetry by observing the $\sqrt{3}$-Au structure in the off-zone imaging mode which will allow the individual atoms of the gold trimers to be resolved. Results from these experiments as well as a detailed analysis of the interaction of the $\sqrt{3}$-Au domains with bulk defects will appear in a separate publication [39].

Also in Table 2 are the $\sqrt{3}$-Au MTLTT parameters from the data sets fitted separately and only the diffuse spot data sets (#1 and #2) fitted simultaneously. Typically, in our diffraction structure analysis, data from at least two different crystal tilt and thickness sets are matched to the proposed structure to eliminate possible artifacts. In such cases combining the sets gives a lower χ^2 than if each set was fitted separately. However, as the χ^2 values in Table 2 show, sets fitted individually have better χ^2 values and substantially different final parameters indicating that the first/second and the third data sets come from slightly different structures. The major difference is that the third data set (sharp spots) has a 3.5° rotation of the gold trimers while the first two sets (diffuse spots) have essentially no gold trimer rotation within experimental errors. This variability of the gold trimer rotation angle is in agreement with the large value of the fitted gold Debye–Waller (DW) term given in Table 2. In other studies [28,40] we have found that the DW term for surface atoms in a well-ordered surface structure typically only increases by a factor of two times its bulk value. This increase is attributable to the increase in the thermal component of the Debye–Waller term since atoms near the surface have added freedom to vibrate. However, the gold DW term in the $\sqrt{3}$-Au structures typically increased to roughly three times its bulk value suggesting the possibility of substantial static surface disorder. This rather large

Table 2
Parameters found for the χ^2 fit of MTLTT model to the $\sqrt{3}$-Au combined and individual diffraction data sets

	MTLTT parameters for the data sets included in the fit					Corresponding bulk Si or Au values
	1,2,3	1,2	1	2	3	
χ^2 Values of fits						
Fitting each set alone			2.14	2.44	2.61	
All sets [a]	2.76		2.57	2.77	3.03	
Sets 1 and 2 [a]		2.31	2.16	2.64		
Trimer values						
Au–Au 1st layer (Å)	2.71	2.78	2.78	2.79	2.67	
Trimer Rot. theta (degrees)	1.94	0.59	0.81	−0.72	3.57	
Si–Si 2nd layer	2.86	3.05	3.10	3.21	2.76	
Theta	3.39	7.65	8.29	2.52	2.50	
Si–Si 3rd layer	3.69	3.71	3.71	3.78	3.69	
Theta	0.84	0.61	0.79	−0.17	0.91	
Si–Si 4th layer	3.80	3.90	3.81	3.82	3.81	3.84
Theta	0.23	−0.02	0.14	0.09	0.20	0.00
Values of the gold trimer center to nearest silicon atom vector V						
Au trimer cen-Si (Å)	2.62	2.67	2.68	2.49	2.64	2.22
Theta (degrees)	9.76	6.24	5.57	6.43	11.04	0.00
Gold to silicon x–y plane projected distances shown in Fig. 2						
Au–Si #1 (Å)	2.07	2.17	2.20	1.99	2.09	2.22
Au–Si #2	2.50	2.48	2.46	2.38	2.49	2.22
Au–Si #3	2.55	2.41	2.40	2.58	2.60	2.22
Debye–Waller terms						
Au 1st layer (Å^2)	3.30	2.64	2.48	4.94	3.72	1.00
Si 2nd layer	0.47	3.68	3.60	3.84	0.47	0.46
Calculated surface coverage of structure						
Coverage Domain 1 (%)			53.1		28.1	
Coverage Domain 2			51.7		26.1	
± Error in coverage estimate			28.8		15.7	

[a] When the data sets are fitted simultaniously, the χ^2s reported in the single set columns are the χ^2s of each corresponding set fitted to that combined set structure.

gold Debye–Waller term is in general agreement with the MEIS results [1]. In this case, the Debye–Waller term is given by [41]

$$S(\mathbf{g}) = S_0(\mathbf{g})\sum_h \delta(g - h/a)\exp\{-\pi^2[b^2g^2 + (\mathbf{g}\cdot\Delta)^2]\}, \quad (2)$$

where S is the average structure factor associated with beam $\mathbf{g}$, S_0 is the structure factor without local atomic disorder, a is the lattice parameter, b^2 is the mean-squared amplitude of the thermal vibrations, and Δ the static mean displacement vector of the atoms. If we assume the static displacements to be isotropic, Eq. (2) becomes:

$$S(\mathbf{g}) = S_0(\mathbf{g})\sum_h \delta(u - h/a)\exp\{-\pi^2[(b^2 + \Delta^2)\mathbf{g}^2]\}, \quad (3)$$

where the quantity $(b^2 + \Delta^2)$ is the Debye–Waller term reported in Table 2. An anisotropic fit of the Debye–Waller terms was tried in an attempt to isolate the static portion, but the results were inconclusive for the reasons mentioned below. The DW term for the second silicon layer stayed surprisingly close to its bulk value for the average structure and the sharp spot structure indicating a well ordered and fairly tightly bonded layer, while

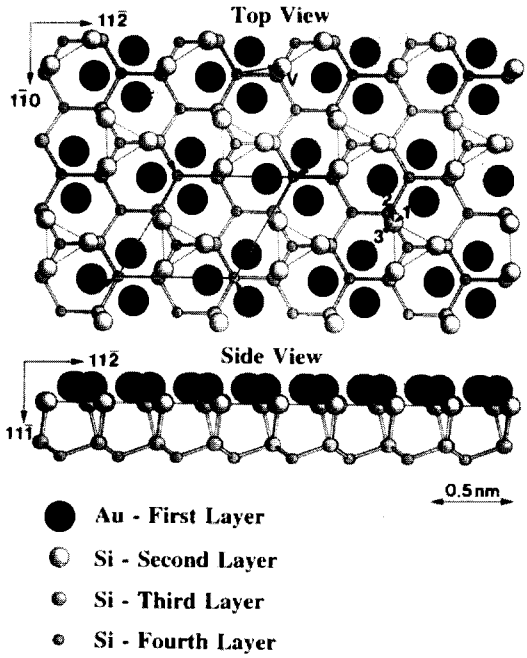

Fig. 2. Top view schematic diagram of the average Si(111)-($\sqrt{3}\times\sqrt{3}$) Au atomic structure corresponding to the three data set combined parameters given in the first column of Table 2. The primitive unit cell is marked with lines and arrows in the lower left portion of the schematic. Three x–y projected gold-to-silicon spacings are shown in the lower right. The utility of the vector **V** (shown above the primitive cell) from the gold trimer center to the second layer silicon atom is discussed in the text.

it rose to several times its bulk value for the diffuse spot structure. Although the DW terms should not be given too much credence (especially the silicon DW term since the χ^2 is not very sensitive to this parameter), their generally high values, interpreted from the point of view of static disorder, do make sense in terms of trimer rotation, the relatively small size of the surface domains, and the discussion of the domain walls below. Because of the strong coupling between the Debye–Waller (DW) term and the occupancy (discussed in the beginning of this section), the occupancy of atoms for all the layers of the model was held at one while the DW terms were allowed to increase above their bulk values. This approach is justified by X-ray results [20] and by Figs. 3a and 3b, which show a regular pattern of dark triangular features in the centers of the indicated surface domains, partial occupancy

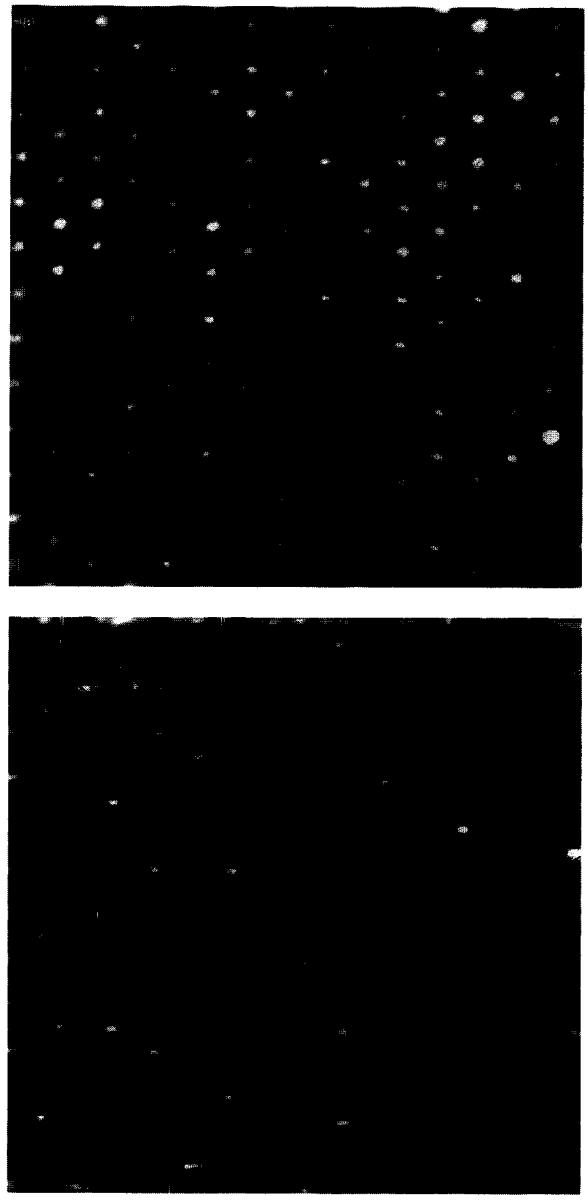

Fig. 3. (111) zone axis high resolution images of the Si(111)-($\sqrt{3}\times\sqrt{3}$) Au surface in which the gold trimers appear as dark triangles showing the structure has local threefold symmetry especially at the centers of the marked polygons. The orientation of the triangles appears to change in (b) because of the structure beams' interaction with Si (1 × 1)-type beams which are stronger in (b) than in (a). The lines outlining the Si(111)-($\sqrt{3}\times\sqrt{3}$) Au domains are more guides for the eye rather than strict delineations of the extents of the domains.

of gold sites would appear as non-threefold distortions of these central features. Lack of threefold features at the very edges of the domains and in the domain walls does not relate to the gold occupancy of the $\sqrt{3}$-Au structure itself since the domain walls do not contribute to the diffraction intensity. If gold is missing in these regions then the *total* gold coverage of the surface would be less than one monolayer while the regions generating diffraction intensity (the central portions of the domains) still have a coverage of exactly one. As mentioned at the beginning of this section, more robust fitting of the Debye–Waller/occupancy parameters (including anisotropic DW term fitting) would require sampling surface structure beams at even higher angles than in this study. While analyzing larger data sets is possible in terms of computational power, we are presently signal-to-noise ratio limited for very weak beams because of the inelastic scattering background.

The diffraction-based evidence for two different $\sqrt{3}$-Au surface phases is also supported by high resolution images. Figs. 4a and 4b are HREM on zone images showing two regions of the $\sqrt{3}$-Au surface with different diffraction spot diffuseness levels. Both Figs. 4a and 4b have been noise filtered, have had the bulk (220) beams eliminated and the 1×1-type beams attenuated to enhance information from the lowest order $\sqrt{3} \times \sqrt{3}$ (10)-type beams. The top halves of the insets are the corresponding power spectra of Figs. 4a and 4b before low pass filtering while the bottom halves are experimental diffraction patterns from similar regions (to the right of the insets are eight times enlargements of the indicated beams). While the $\sqrt{3}$ spacing (6.65 Å) fringes are present in both, Figs. 4a and 4b have distinctly different morphologies. Fig. 4b essentially shows that sharper $\sqrt{3}$-Au diffraction spots correspond to a tighter packing of $\sqrt{3}$ spacing crossed fringe regions, which could indicate a tighter packing of surface domains, illustrated by the sharp transition between the lighter and darker $\sqrt{3}$-Au feature regions outlined, for instance, in the upper left region of Fig. 4b versus the wider region of lower contrast surrounding the $\sqrt{3}$-Au domain outlined in Fig. 4a. Since the surface regions shown in Figs. 4a and 4b are only 97 nm apart, different researchers could be

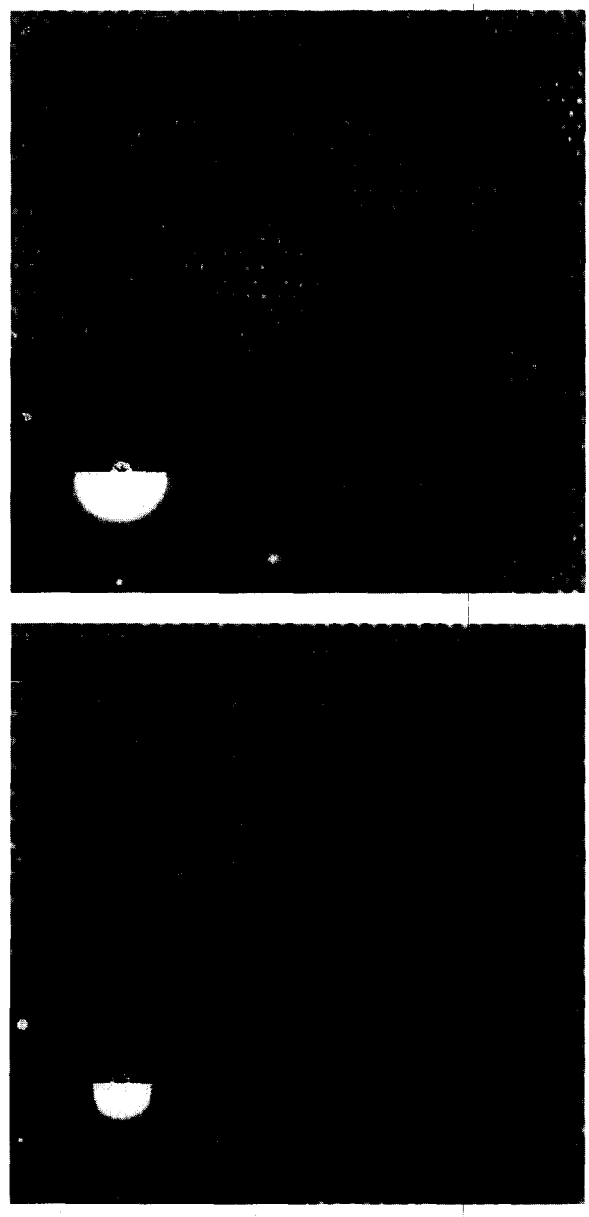

Fig. 4. Strongly low pass filtered HREM (111) zone axis images showing two regions of the $\sqrt{3}$-Au surface. (a) is from a region with diffuse diffraction spots as shown by its corresponding power spectrum (before low pass filtering) in the top half of the inset. (b) is from a region with sharp spots as shown by its inset. The bottom halves of the insets are experimental diffraction patterns from data sets 1 and 3, respectively, while to the right of each main inset are 8 × magnifications of the corresponding arrowed spots. An outlined $\sqrt{3} \times \sqrt{3}$ domain in the upper left of (a) is surrounded by regions of lower fringe contrast indicating a domain wall, the rough boundary of which is indicated by the lines to the right of the surface domain. Note the difference between the wider surface domain walls of (a) versus the narrower walls between domains in (b) indicated, for instance, by the line between two domains in the upper left of (b).

studying subtly different structures depending on the exact surface preparation conditions used, a fact that Kuwahara and coworkers have already partially alluded to Ref. [23].

We will now highlight the key results of the three data sets fitted simultaneously to the MTLTT structure. Given the above facts this structure can only be considered an average structure of the $\sqrt{3}$-Au surface. Results from separately fitted data sets give a better indication of the structures of the diffuse and sharp diffraction spot surfaces. Important differences between these results, the average structure results, and literature results will be noted where appropriate. The average structure in general matches MTLTT Structure 1 proposed by Chester and Gustafsson in which the gold and silicon trimers rotate in the same direction. The first layer of the structure consists of gold atoms near the T_1-type sites forming trimers centered at and rotating about the H_3-type sites. The gold trimers rotate by an average 1.9° with a Au–Au gold interatomic distance of 2.71 Å. The second layer of the structure consists of silicon trimers rotated by 3.4° about their centers (in the convention used by Chester and Gustafsson) with a Si–Si interatomic distance of 2.85 Å. Since TEM is not sensitive to displacements parallel to the electron beam the z-axis distance between the gold and silicon layers could not be measured. Therefore, the interatomic distances quoted between the gold and the silicon are x–y plane projected distances. For reference, the literature values for the gold-to-silicon layer distance include 1.7 Å from MEIS [1], 0.3 Å and 0.7–2.0 Å from ICISS, Refs. [17] and [18], respectively, 0.9 Å from X-ray diffraction [23], 0.56 Å from total energy calculations and LEED [21,22]. (The X-ray diffraction height result is used for the side views of Fig. 2 and Fig. 5.)

Before continuing this discussion of the results, an important point concerning the structure parameters needs to be made. In the MTLTT model there are two "twist" centers and care must be taken to choose appropriate parameters when comparing different structure models. The structure description parameters used by Chester and Gustafsson [1] are the interatomic distances within a layer and the rotation angles of the gold and silicon trimers about their individual centers. While the Au–Au interatomic distance plus the gold trimer rotation angle are good descriptions of the gold layer of the structure, second layer silicon displacements only along the line joining gold trimer centers would generate a silicon "twist" about the local silicon threefold center even though true silicon trimers have not formed, for example as in the CHCT model [21]. A better description of the position of the second layer silicon with respect to the gold is the vector from the gold trimer center to the second layer silicon atom (shown by the arrow V in Fig. 2) measuring the angle in terms of the deflection of silicon from its bulk site. This parameter's advantages are a ready display of the degree of silicon trimerization in terms of the vector angle while also showing the general displacement of the silicon from the gold in terms of the vector magnitude. These vector parameters for all structures are given in Table 2. We can see that in all cases the silicon atom to gold trimer center distance remains roughly constant but the angle of the actual silicon site from its bulk position, while always at least 5°, increases to 11° when the gold trimers rotate. The fact that both the first layer Au–Au and second layer Si–Si interatomic spacings contract somewhat for the rotated gold trimer data set is also worth noting.

Table 3 shows a comparison of the present work's average structure model to recent gold-trimer-based models, which propose lateral sites for both the gold first layer and the silicon second layer. (As several authors [1,17,20–22] have concluded, 2/3 ML honeycomb-based models can be excluded from consideration.) Table 3 provides silicon-to-gold trimer center values mentioned above for all models as well as the silicon trimer rotation parameters of Chester and Gustafsson for comparison. All gold-to-silicon spacings are x–y plane projections based on the parameters quoted by the respective authors (all parameters used for the X-ray results are based on the parameters quoted in Table 3 of Ref. [20]). The gold trimer center to silicon atom spacing shows good agreement between the X-ray, dynamical LEED, total energy calculation, and the present study's average model. The fact that the silicon position deflection angle can vary between 5° and 11° agrees well with the grazing incident angle X-ray models. While not

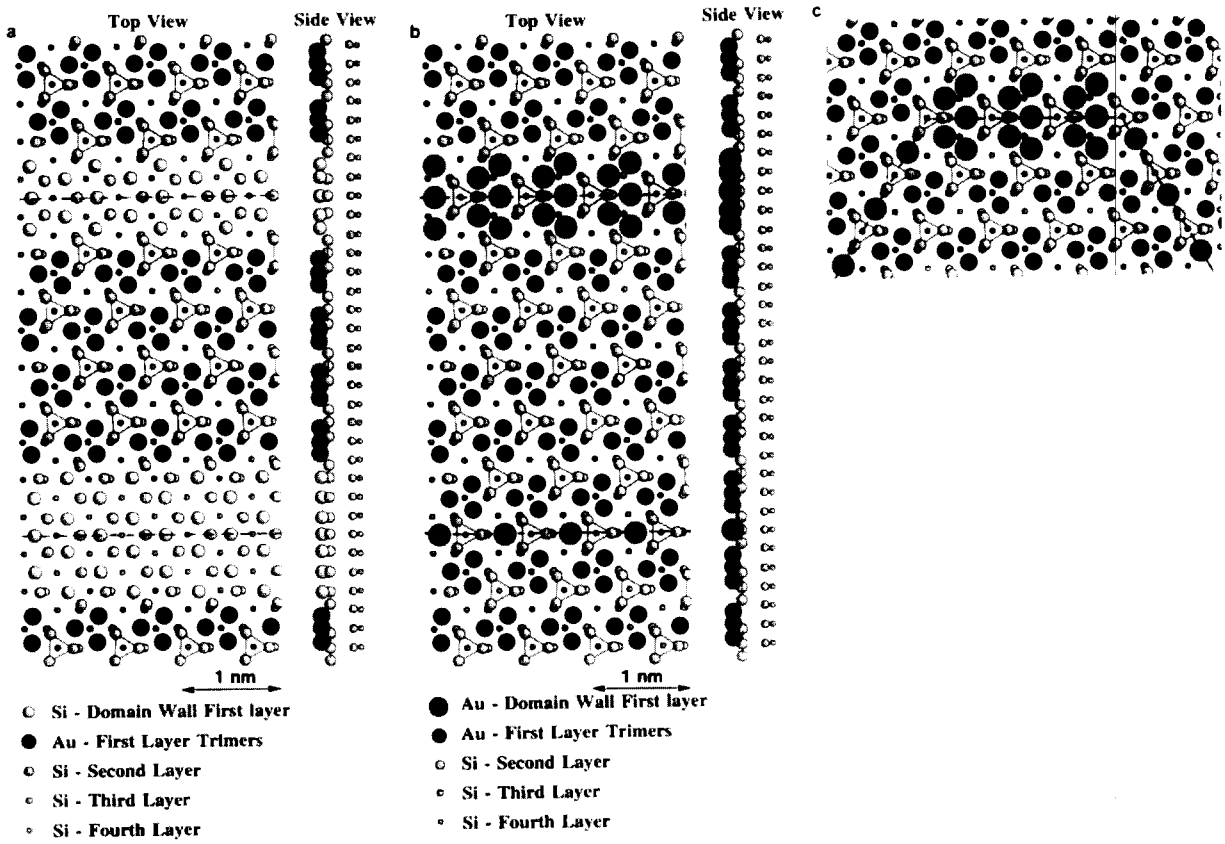

Fig. 5. (a,b) Top and side view schematics of the atomic structures of four possible $\sqrt{3}$-Au surface domain walls, which agree with diffraction and HREM data, the dashed lines show the mirror planes associated with the domain walls. (a) Shows two-vacancy-type domain walls consisting of a silicon double layer providing continuity between $\sqrt{3}$-Au domains while (b) shows "neutral"-type domain walls with 1.0 ML total gold coverage. (c) Schematic diagram of a turning domain wall incorporating both types of proposed "neutral" domain wall structures. Note the continuity of the trimered silicon layer across the domain walls shown in (b) and (c) by the lines connecting the trimer Si atoms.

included in Table 3, the lateral spacing X-ray diffraction results of Kuwahara et al. [23] essentially agree with our results since they found a gold–gold interatomic distance of about 2.7 Å and no trimer rotation within $\pm 3.0°$ for a diffuse LEED diffraction spot structure. Where our results disagree with the three studies is in the gold trimer rotation. Although we agree with the MEIS results [1] in confirming that the gold trimers do rotate we do not agree with them in the degree of rotation. The present results are most at odds with the dynamical LEED results [22] where no gold or silicon trimer rotations were reported for "sharp, high quality spots". The LEED analysis and the total energy calculation results concluded that the $\sqrt{3}$-Au structure must obey p3m1 symmetry while we conclude the structure has two domains of local p3 symmetry, with a small average domain size and a sufficient number of domains of both types in a given area this will give results identical to a p3m1 symmetry since the diffraction intensities will statistically balance. A clear example of this diffraction intensity summing of two p3-type domains is given by Akiyama et al. [19] in a TEM study of Si(111)-($\sqrt{3} \times \sqrt{3}$) Pd. In this study dark field images using the strongest surface related diffraction spots showed consistent intensity differences between the two types of domains arising from Pd trimers twisted roughly 6° with respect to the bulk.

Table 3
Comparison of parameters for different recent models of the Si(111)-$\sqrt{3}\times\sqrt{3}$) Au surface.

References	TED (present) Avg.	X-ray [17]		MEIS [1]		TEC [18]	LEED [19]
		III-Si	III-Au	Str. 1	Str. 2		
Trimer values							
Au–Au (Å)	2.71	2.80	2.80	3.00	2.90	2.83	2.80
Theta (degrees)	1.94	0.00	0.00	12.00	12.00	0.00	0.00
Si–Si 2nd layer	2.86	2.89	2.88	3.20	3.20	3.50	3.50
Theta	3.39	4.84	5.64	18.00	−17.00	11.40	11.66
Values of gold trimer center to nearest silicon atom vector							
Au cen-Si (Å)	2.62	2.65	2.67	2.94	2.08	2.68	2.69
Theta (degrees)	9.76	8.86	8.74	2.19	18.48	0.00	0.00
Gold-to-silicon x–y projected distances							
Au–Si #1 (Å)	2.07	2.06	2.08	2.85	1.73	2.34	2.34
Au–Si #2	2.50	2.56	2.57	2.27	2.09	2.34	2.35
Au–Si #3	2.55	2.45	2.43	2.07	3.20	2.34	2.34

To check the robustness of the average structure analysis, several variations of the starting structure were studied. Changing the number of layers allowed to relax produced the following χ^2 values versus relaxation depths: 4.54 for no relaxation (just the gold can move), 2.88 for one layer (just the gold and second layer silicon can move), 2.78 for two silicon layers, and 2.76 for three silicon layers with χ^2 remaining constant for deeper relaxations. These results, which provide a good picture of the x–y plane silicon displacements with depth, are in agreement with the X-ray diffraction results of Kuwahara et al. [23] which show small z-axis silicon displacements for the third and fourth silicon layers. Table 2 gives the average structure trimerization of third and fourth layers of the structure. If Chester and Gustafsson's Structure 2 with counter-rotated silicon and gold trimers is used as a starting point the structure will move back to Structure 1. If the gold and silicon trimers are not allowed to rotate we essentially have a CHCT model, this fitted structure has a χ^2 of 3.50 and the gold DW term rises to four times its bulk value versus three times its bulk value in our proposed structure. Clearly the rotation of at least one set of trimers must be present in the structure. If silicon trimers can rotate but the gold trimers cannot, a structure very similar to the one proposed by Dornisch et al. [20] has a slightly increased χ^2 of 2.82 (for our data) and a slightly increased gold DW term. If the gold trimers are locked with no rotation for the fitting of third data set alone (the sharp spot set with normally the largest gold rotation) the resulting χ^2 is 3.03 versus 2.61 if the gold trimers rotate.

The rotation of the gold trimers could explain certain STM $\sqrt{3}$-Au coverage results first seen by Nogami et al. [8] and quantified by Takami et al. [9]. To explain this, we note that the theoretical work of Ding and coworkers [21] predicts that the gold trimer will have electronic states corresponding to the single bright feature per $\sqrt{3}\times\sqrt{3}$ unit cell seen in STM. This analysis was based on the CHCT model, which roughly corresponds to our diffuse diffraction spot structure (usually seen at lower coverages) in having no gold trimer rotation. However, STM [8,9] results show that single bright feature per unit cell regions covered the surface most completely in the lower gold coverage regime (roughly 0.7 to 0.8 ML), at higher gold coverages (0.9 to 1.0 ML) regions with a $\sqrt{3}\times\sqrt{3}$ LEED pattern and more complicated STM features covered the surface [9]. The trimer rotation moves the gold out of higher symmetry sites with respect to the bulk, possibly breaking some degeneracies of electronic states and leading to a more complicated STM image. The rotated gold trimer structure, which the present work associates with

the sharp $\sqrt{3}$-Au diffraction spots (commonly seen at higher gold coverages), could be this second type of $\sqrt{3}$-Au surface seen by STM.

Another clue to the electronic nature of this structure comes from the scattering potentials used in the fit. X-ray scattering potentials for Au^+ were used, the corresponding χ^2 for neutral gold atoms was significantly higher, 3.92 for the average structure results with essentially no change in the atomic positions. This result agrees nicely with the results of Dobrodey et al. [2] who in a nonempirical cluster study predict a 0.8 electron charge transfer from the gold to the silicon. Electron charge transfer away from the gold also agrees in general with the reduced gold-to-gold interatomic distance in the trimers (2.72 Å versus 2.88 Å for bulk gold) and could be the driving force behind the gold coverage dependent morphology changes seen in this system. We will return to the charge transfer issue after discussing the surface domain walls. The significant drop in χ^2 between charged and neutral gold also clearly indicates the need to consider charge transfer in diffraction analysis of these types of structures, an analysis of the $\sqrt{3}$-Au structure with proper charge balance could yield an even lower χ^2 but to the best of our knowledge X-ray or electron scattering potentials for Si^- are not available.

Given the possibility of at least two different $\sqrt{3}$-Au surface structures (one with diffuse diffraction spots and one with sharp ones), the measurement of the actual coverage of the surface with a $\sqrt{3}\times\sqrt{3}$ periodic structure becomes more critical. Hence in addition to the estimate of the amount of gold evaporated (roughly 0.7 ML from a quartz crystal microbalance, which leads to 70% $\sqrt{3}$-Au structure coverage of the surface), two independent estimates of the structure's coverage were obtained in this study. Stereology of regions of $\sqrt{3}$ spacing fringes in bright field TEM images from diffuse spot diffraction spot regions were used to obtain an average $\sqrt{3}$-Au domain diameter of 6.8 ± 1.9 $\sqrt{3}$-Au unit cell spacings (45.2 Å $\pm$12.6 Å) with a surface coverage of 45%. The measurement involved over 130 domains with the domain extent being defined by the visibility of $\sqrt{3}$ fringes running in at least two of three possible directions. For example in Fig. 4a (a high resolution image which has been low pass filtered to the point where it is essentially a bright field image) some areas have fringes going in two directions crossing each other while other areas have fringes running in only one direction, i.e., contrast from the other directions is greatly reduced. If these single direction fringe regions are included in the coverage measurement the ($\sqrt{3}\times\sqrt{3}$) coverage of the surface rises to roughly 75%–90%. The other coverage estimation method is based on comparing the calculated absolute diffracted beam intensities to the measured absolute beam intensities, these coverage values obtained for the first and third data sets are given in Table 2. This approach is similar to the scattering yield approach used in the MEIS study [1]. Since the absolute structure beam intensities were not measured directly, the absolute intensities were estimated by comparing the simulated bulk beam intensities with the measured bulk beam intensities to obtain a mean intensity scaling factor. This scaling factor was then applied to the measured surface beam intensities, after which a comparison of the simulated and scaled measured surface structure beams yields the coverage estimate; the percentage of the surface contributing to the intensity of the diffracted beams. This measurement, which in principle can provide very accurate structure coverage measurements for well-fitted bulk simulations, is for these data sets prone to a large source of error because the intensities of the transmitted and strongest bulk beams were not measured. As a result, only a visual fit could be used to obtain roughly the correct crystal tilt and thickness parameters. (Without the strongest bulk beams a multislice fitting algorithm for the crystal tilt and thickness will fall into incorrect local minima.) Using these two unoptimized bulk parameters then leads to a fairly broad distribution of intensity scaling values and hence a large (55%) standard deviation for their mean, this deviation then propagates to the coverage measurement. It should be emphasized, however, that since the coverage estimates fall within an order of magnitude of the expected values (the coverage estimates are 105% for the diffuse spot set and 54% for the sharp spot set compared to 70% from the microbalance and 45% from stereology) there are no serious overfittings or other major discrepancies occurring

in the diffraction analysis as would be indicated by much higher or much lower values. Due to the likely presence of numerous surface steps on the TEM sample and the possible effects of electron beam damage, we do not expect these absolute coverage estimates to be as accurate in finding the $\sqrt{3}$-Au "saturation coverage" as the results of Chester and Gustafsson [1] using MEIS scattering yields (0.85 ML) or the detailed STM studies of Nogami et al. [8] and Takami et al. [9] in which the domain wall sizes were determined as a function of coverage in 0.1 ML steps. The above results simply show that the majority of the surface was involved in generating the diffraction intensities upon which we base our model.

The absence of the dark triangular $\sqrt{3}$-Au features near the domain walls in Fig. 3a and especially in Fig. 3b deserves some attention. Bearing in mind that these are on zone images there are only two possible interpretations of the absence of the features: (1) the domain walls are vacancy type with respect to gold and hence there is no gold to generate a feature, or (2) the gold–gold spacings close to and within the domain walls must be very similar to the silicon 1×1 spacing (3.84 Å). We will return to the second possibility in a moment. Grain boundary theory in general predicts that the domain walls would be of vacancy type, especially for lower gold coverages (0.5–0.85 ML). That is, given that the domains themselves have a gold coverage of 1.0 ML (as we noted earlier, Figs. 3a and 3b rule out partially occupied trimer gold sites) the only way for $\sqrt{3}$-Au to cover the entire surface at lower coverages is for the domain walls to be vacancy type. Two possible vacancy-type domain wall structures are shown in Fig. 5a and are based on our recent results [40] from the 0.4 ML gold coverage Si(111)-(5×2) Au surface. In that study we found that the (5×2) Au surface consists of an expanded silicon double layer filling the gaps between linear rows of a missing top layer like gold silicon structure. The two vacancy-type walls we propose are similar in some ways to two of the three domain walls outlined by Chester and Gustafsson (in figure 14 of Ref. [1]), which are based solely on surface structure to bulk registry considerations. However, we propose that the specific nature of the vacancy-type walls is essentially a silicon double layer providing surface continuity between the $\sqrt{3}$-Au domains. The $\sqrt{3}$-Au vacancy-type domain walls are line defects in the $\sqrt{3}$-Au surface, which can be considered one-dimensional analogies to Lave phases. Vacancy-type domain walls and the relatively small average domain size lead one to conclude that, at least for lower gold coverages, the $\sqrt{3}$-Au surface is a two-dimensional surface solution which has different average structure parameters at different gold coverages. The coverage range of this surface solution is shown schematically in Fig. 6.

The problem with a vacancy-type domain wall picture for the higher range of gold coverages (0.9–1.0 ML) is that Nogami and coworkers [8] saw that the density of domain walls increases with increasing gold coverage. This means a domain wall which incorporates gold in its structure must be present for gold coverages near 1.0 ML. We now focus on the nature of this 1.0 ML "neutral" (versus vacancy, heavy or superheavy) type of domain wall. To understand the 3.84 Å gold spacing interpretation mentioned above, note that in on-zone imaging, multiple scattering enhances the bulk forbidden/surface allowed, (1×1) type, 3.84 Å spacing beams as well as the bulk beams [42]. As a result, in on zone imaging when even strong scatterers such as gold have interatomic spacings

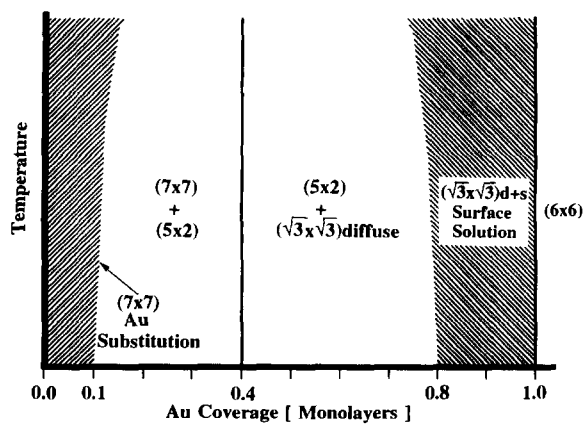

Fig. 6. Generalized schematic surface phase map of the Si(111) Au system up to one monolayer. The surface solution coverage region of the $\sqrt{3}$-Au structure is indicated by the lines between 0.8 and 1.0 ML. The curves near 0.1 and 0.8 ML are not drawn as vertical lines to illustrate various effects such as the change of solubility with temperature.

close to bulk or surface termination related spacings their scattering will be washed out by the stronger signal. Our results for the Si(111)-(5 × 2) Au structure [40] show that a 3.84 Å domain wall gold-to-gold spacing interpretation is quite possible. Along with this fact what can else we infer about the "neutral" domain wall structure, given the structure of the domains themselves? If the gold trimers alone are considered, a $\sqrt{3} \times \sqrt{3}$-type structure on a (111)-oriented surface allows three possible registries of the surface structure with the bulk. However, the trimerization of the second layer silicon atoms generates two domains in this layer with a mirror plane between them. A simple first layer gold trimer registry shift is no longer allowed unless it is accompanied by a second silicon layer domain change. Of the six possible registry shift/domain change combinations possible (all of which have the same 1 ML local gold coverage as the domain structure, hence the "neutral" description) only the two shown in Fig. 5b agree with the fitted second silicon layer Debye–Waller term for the data sets associated with higher coverages. Recall that the second layer silicon DW term of the average structure and the sharp diffraction spot set structure is very close to the bulk silicon value, indicating a well-ordered layer. Both domain walls configurations in Fig. 5b have the second silicon layer trimer pattern intact across the entire surface as shown by the triangular pattern of lines connecting the trimered silicons. The other four combinations cause either zipper or W-shaped distortions in the second layer silicon trimer pattern. The domain wall internal 3.84 Å gold-to-gold spacing observation and the tight packing of the domains in Fig. 4b favor the single gold atom type of domain wall, but the five gold atom type is not ruled out as long as all five atoms in the W-type configuration settle close to the T_1 sites. Both types of boundaries can only change direction so that the domain walls are 60° apart and one type of wall can change to the other with a 120° angle between walls as shown in Fig. 5c. These turning rules also apply to the vacancy-type domain walls in Fig. 5a. The behavior of all these domain walls in turning and changing type agrees with the observations of Nogami et al. [8].

If one assumes that the two types of domain walls have different energies, then the incommensurate to commensurate transition from the $\sqrt{3}$-Au structure to the Si(111)-(6 × 6) Au structure ((6 × 6) Au hereafter), reported by several authors [6–10], which occurs at and above 1 ML and below roughly 300°C can be understood in terms of the exclusion of one type of domain wall in favor of the other plus a shrinking of the domains. In conjunction with STM images [8] of (6 × 6) Au this would lead to the possible model shown in Fig. 7a. While the TED pattern simulated from this model (Fig. 7b) shows features qualitatively similar to (6 × 6) Au TED patterns in the literature (figures 3 and 8c of Ref. [7] for example) this model is only suggested as a starting point for future work. We speculate that the ability of the Si(111)-(6 × 6) Au structure to absorb gold up to about 1.5 ML [8–10] is partially related to the domain walls, if the gold atoms along the domain walls were to shift toward the sites marked with ×'s in Fig. 7a equivalent × sites on the opposite side of the domain wall for 0.25 ML more gold would be available in the now "heavy"-type domain walls.

To close our discussion of the $\sqrt{3}$-Au system we hypothesize that charge transfer changes in the structure with increasing gold coverage are the key to understanding the domain wall behavior and hence the morphology changes. As alluded to earlier, significant transfer of charge away from the gold can explain why the gold-to-gold spacing in the trimers is less than in bulk gold. The contraction of spacings in the gold trimers causes these trimers to put compressive stress on the normally tensile stressed silicon (111) surface. The system does not reach a balance however, as shown by the fairly small surface domains. The largest charge transfer and therefore the best possible stress balance would occur at the lowest gold coverages. As gold coverage increases the charge transfer becomes less pronounced and more domain walls (essentially line defects) form as the surface's stress relief mechanism. From this hypothesis one would expect that with increasing gold coverage the gold-to-gold interatomic spacing would increase and the neutral Au scattering potentials fit χ^2 relative to the Au^+ fit χ^2 would decrease with increasing gold coverage. While the χ^2s show the correct

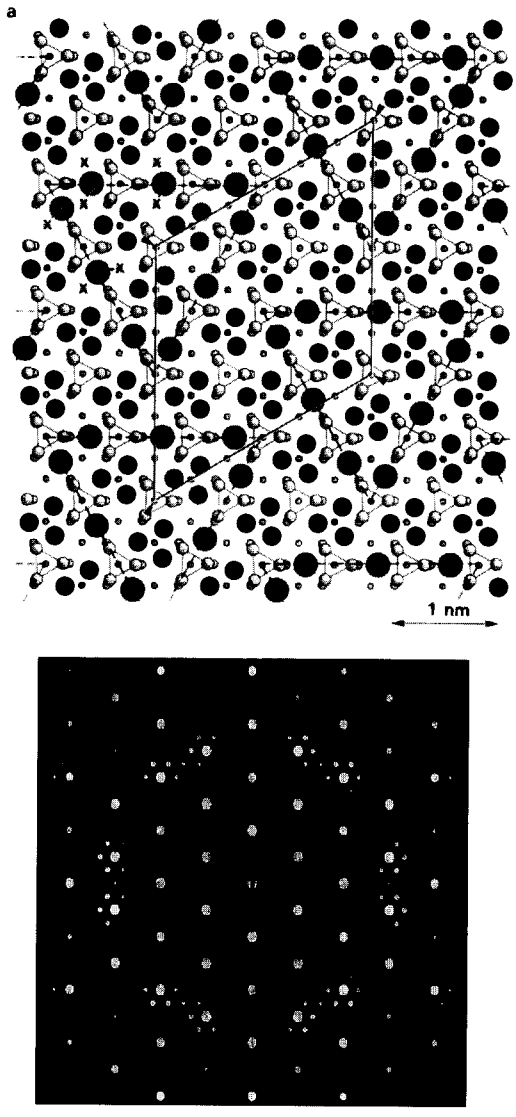

Fig. 7. (a) Top view schematic diagram of a model Si(111)-(6×6) Au structure based on the results of the present study and STM images [8] with the primitive unit cell indicated by solid lines and arrowed corners and the domain walls by dashed lines. If the arrowed domain wall gold atoms in the upper left move in the indicated directions into the sites marked "×" then the other "×" sites could accommodate more gold atoms. (b) Simulated on zone TED pattern based on the proposed structure with the transmitted and one (220)-type beam indicated.

trend between the diffuse and sharp diffraction spot results, the stronger potential proof, the gold-to-gold spacing, shows the opposite trend: decreasing in going from the diffuse spot structure to the sharp spot structure. Considering the limited number of measurements and the inherent averaging nature of the measurement, more work is needed to prove or disprove this proposal.

5. Conclusions

We have shown that while the MTLTT model with the first layer gold and second layer silicon trimers rotating in the same direction gives the best description of the Si(111)-($\sqrt{3}\times\sqrt{3}$) Au structure, the parameters of this model vary significantly with the degree of diffuseness of the diffraction spots, and that charge transfer from the gold to the silicon occurs. Sharper diffraction spots have more gold and silicon trimer rotation and shorter trimer interatomic distances while more diffuse diffraction spots have essentially no gold trimer rotation, and longer interatomic distances. This correlates to HREM images of the two regions which show tighter packing of domains for the sharper diffraction spots. The role of two proposed vacancy-type domain walls has been postulated in explaining the solid solution like behavior of the system in the lower gold coverage regime. Two possible "neutral" domain wall structures have been proposed for the surface when near 1 ML of gold based on diffraction and HREM data. One of these proposed domain walls is an integral part of a proposed Si(111)-(6x6) Au structure.

Acknowledgements

The first author would like to thank Professor Jun Nogami for his helpful discussions, Ganesh Jayaram for his assistance in some of the microscopy of this structure, and Dan Grozea for his assistance in the analysis of some of the diffraction patterns. This work was supported by the Air Force Office of Scientific Research under Grant #F49620-92-J-0250.

References

[1] M. Chester and T. Gustafsson, Surf. Sci. 256 (1991) 135.
[2] N.V. Dobrodey, L.I. Ziegelman, V.G. Zavodinsky and I.A. Kuzanov, Surf. Rev. Lett. 1 (1994) 273.
[3] T. Takahashi and S. Nakatani, Surf. Sci. 282 (1993) 17, and references therein.
[4] J.F. Jia, R.G. Zhao and W.S. Yang, Phys. Rev. B 48 (1993) 18109.
[5] H.E. Bishop and J.C. Riviere, Brit. J. Appl. Phys. 2 (1969) 1635.
[6] K. Higashiyama, S. Kono and T. Sagawa, Jpn. J. Appl. Phys. 25 (1986) L117.
[7] S. Takahashi, Y. Tanishiro and K. Takayanagi, Surf. Sci. 242 (1991) 73.
[8] J. Nogami, A.A. Baski and C.F. Quate, Phys. Rev. Lett. 65 (1990) 1611.
[9] T. Takami, D. Fukushi, T. Nakayama, M. Uda and M. Aono, Jpn. J. Appl. Phys. 33 (1994) 3688.
[10] J. Yuhara, M. Inoue and K. Morita, J. Vac. Sci. Technol. A 10 (1992) 3486.
[11] S. Ino, Jpn. J. Appl. Phys. 16 (1977) 891.
[12] F. Salvan, H. Fuchs, A. Baratoff and G. Binning, Surf. Sci. 162 (1985) 634.
[13] Ph. Dumas, A. Humbert, G. Mathieu, P. Mathiez, C. Mouttet, R. Rolland, F. Salvan and F. Thibaudau, J. Vac. Sci. Technol. A 6 (1988) 517.
[14] T. Hasegawa, K. Takata, S. Hasaka and S. Hosoki, J. Vac. Sci. Technol. A 8 (1990) 241.
[15] A. Shibata, Y. Kimura and K. Takayanagi, Surf. Sci. 273 (1992) L430.
[16] G. Lelay and J.P. Faurie, Surf. Sci. 69 (1977) 295.
[17] K. Oura, M. Katayama, F. Shoji and T. Hanawa, Phys. Rev. Lett. 55 (1985) 1486.
[18] J.H. Huang and R.S. Williams, Phys. Rev. B 38 (1988) 4022.
[19] K. Akiyama, K. Takayanagi and Y. Tanishiro, Surf. Sci. 205 (1988) 177.
[20] D. Dornisch, W. Moritz, H. Schulz, R. Feidenhans'l, M. Nielsen, F. Grey and R.L. Johnson, Phys. Rev. B 44 (1992) 11221.
[21] Y.G. Ding, C.T. Chan and K.M. Ho, Surf. Sci. 275 (1992) L691.
[22] J. Quinn, F. Jona and P.M. Marcus, Phys. Rev. B 46 (1992) 7288.
[23] Y. Kuwahara, S. Natani, M. Takahsi, M. Aono and T. Takahashi, Surf. Sci. 310 (1994) 226.
[24] L. Seehofer and R.L. Johnson, Surf. Sci. 318 (1994) 21.
[25] K. Takayanagi, Y. Tanishiro, S. Takahashi and M. Takahashi, Surf. Sci. 164 (1985) 367.
[26] J.M. Gibson, Surf. Sci. 239 (1990) L531.
[27] L.D. Marks, P. Xu and D.N. Dunn, Surf. Sci. 294 (1993) 324.
[28] G. Jayaram, P. Xu and L.D. Marks, Phys. Rev. Lett. 71 (1993) 3489.
[29] L.D. Marks, R. Ai, J.E. Bonevich, M.I. Buckett, D. Dunn, J.P. Zhang, M. Jacoby and P.C. Stair, Ultramicroscopy 37 (1991) 90.
[30] J.E. Bonevich and L.D. Marks, Microscopy 22 (1992) 95.
[31] P. Xu, G. Jayaram and L.D. Marks, Ultramicroscopy 53 (1994) 15.
[32] R.D. Twesten and J.M. Gibson, Ultramicroscopy 53 (1994) 223.
[33] L.D. Marks, R. Ai, T.S. Savage and J.P. Zhang, J. Vac. Sci. Technol. A 11 (1993) 469.
[34] L.D. Marks, P. Xu and D.N. Dunn, Surf. Sci. 294 (1993) 322.
[35] L.D. Marks, Ultramicroscopy 45 (1992) 145.
[36] J.E. Dennis, D.M. Gay and R.E. Welsch, ACM Trans. Math. Software 7 (1981) 348.
[37] L.D. Marks and R. Plass, in preparation.
[38] L.D. Marks, Ultramicroscopy, submitted.
[39] R. Plass and L.D. Marks, in preparation.
[40] R. Plass and L.D. Marks, MSA Proc. 52 (1994) 762; L.D. Marks and R. Plass, Phys. Rev. Lett., submitted.
[41] J.M. Cowely, Diffraction Physics, 2nd ed. (North-Holland, Amsterdam, 1984) p. 257.
[42] P. Xu and L.D. Marks, Ultramicroscopy 45 (1992) 155.